Supplementary Information

Sustainable room-temperature, water-driven conversion of CO_2 to graphitic carbon quantum dots on electride electrodes

Experimental section

Preparation of $LaCu_{0.67}Si_{1.33}$ and Y_5Si_3 NPs

$LaCu_{0.67}Si_{1.33}$ and Y_5Si_3 nanoparticles were synthesized via a previously reported arc evaporation method in an Ar/H_2 atmosphere[1]. $La_1Cu_{0.065}Si_1$ and $Y_5Si_{3.5}$ ingots were obtained using the conventional arc melting method**.** Elemental lanthanum, copper, and silicon for preparation of $La_1Cu_{0.065}Si_1$, and Elemental yttrium, and silicon for preparation of $Y_5Si_{3.5}$, were placed on water cooled copper hearth and arc melted under an Ar atmosphere. The obtained ingots are colored silver and stable in air, and were then transferred into an Ar/H_2 arc evaporation system supplied by Attotec Co., Ltd.. The Ar/H_2 arc realizes extremely high temperature (~10000 °C) in the reaction chamber and can evaporate base materials. The nanoparticles are collected using a stainless-steel filter. During the Ar/H_2 arc evaporation process, Ar and H_2 partial pressures were set to 0.03 MPa and 0.03 MPa, and the flow rates were set to 60 mL/min for each. The arc current was set to 100 A. After finishing arc evaporation, the filter room was detached and transferred into an Ar-filled glove box. Electride NPs were then collected from the filter, avoiding air exposure.

Fabrication of electrode

The electride NPs were mixed with polyvinylidene fluoride (Canrud, China) in a mass ratio of 90:10 with N-methyl-2-pyrrolidone (99.5%, Acros Organics, Belgium) as a solvent to obtain a black slurry. The mixture was stirred for 1 h then heat at temperature 80 ^oC for 10 min to reduce agglomerate. When the mixture is homogeneous, they were coated onto the substrates (1 cm x 1 cm): copper foil (0.1 mm thickness, 99.9999% purity, Alfa Aesar, Thermo Fisher Scientific, USA), nickel foil (0.1 mm thickness, 99.5% purity, Alfa Aesar, Thermo Fisher Scientific, USA), and transparent conductive indium tin oxide glass (ITO) (6 Ω/sq, 20 × 20 × 1.1 mm, JINDON (China). The prepared electrodes were dried in a vacuum oven at 80 °C overnight. Prior to coating, the metallic substrates were prepared by using 800 grit sandpaper to remove the oxide surface.

DFT calculations

Density functional theory (DFT) calculations were performed using the Vienna Ab initio Simulation Package[2]. The electronic exchange-correlation functional was described using the Perdew-Burke-Ernzerhof (PBE) within the generalized gradient approximation (GGA)[3]. The core electrons are handled in the projector augmented wave method, and valence electrons are represented with wave functions based on plane waves[4]. A plane-wave energy cutoff of 520 eV was used for stoichiometric LaCuSi. A Γ-centered Monkhorst-Pack sampling grids with a 12 × 12 × 8 were used for Brillouin-zone integrations[5]. The anionic electron-related DOS was calculated by projecting the wave function onto empty spheres inside a triangular dipyramid (pseudo atoms) of La_3Cu_2, and the radius used for the pseudo atoms was 1.557 Å.

Electrochemical reaction

Firstly, ethanolamine (MEA ≥99%, Carlo Erba Reagents S.r.l., Cornaredo, Italy) solution containing pure or 30%w/w of ethanolamine, 0.4 M of ionic salts (NH_4SO_4 99.5%, Thomas Baker Chemicals Pvt. Ltd., Mumbai, India), 1-Butyl-3-methylimidazolium tetrafluoroborate ([BMIM][BF_4], ≥ 98.5%, Sigma-Aldrich), choline chloride, Loba Chemie Pvt. Ltd., Mumbai, India) and solvent (D_2O, 99.9% Cambridge Isotope Laboratories, Inc. Andover, MA, USA) and de-ionized H_2O was purged with CO_2 (100 cm^3/min, 99.99% Linde) for 1 h until the liquid electrolyte was fully saturated with CO_2 then purged with N_2 (100 cm^3/min, 99.99% Linde) for 20 min to remove physically adsorbed CO_2 species[6]. The reaction performs in H-cell configuration consisting of a three-electrode system including working, reference, and counter electrodes with a potentiostat (Multi Autolab (M204), Metrohm). A Pt plate (5 cm x 5 cm) was used as a counter electrode and the anodic chamber contained 25 cm^3 of the ethanolamine solution with purged CO_2. Ag/AgCl reference was served as the reference electrode and the as-prepared electrode was employed as the working electrode. The cathodic chamber contains 25 cm^3 of the ethanolamine solution with purged CO_2. During the experiment, an electrical current was simultaneously applied at -1, -1.25, -1.5, -1.75, -2.0 and -2.25 for 90 min. Some conditions have CO_2 or H_2 (99.999%, S.I. Technology Co.,Ltd, Bangkok, Thailand) continuously fed with a flow rate of 20 cm^3/min. The stability of the fabricated electrode was studied for 24 hr at -1.5 V. After the electrochemical reaction, the working electrodes were collected and washed with DI-water before further analysis. The electrodes were characterized through linear sweep voltammetry (LSV) measurements spanning a potential range of 0 to −3 V versus Ag/AgCl, employing a scan rate of 5 mV s^{-1} for

finding the onset potential. The electrolyte solution was collected and subjected to analysis to identify and quantify liquid products by ^{1}H NMR.

Separation method for graphitic carbon quantum dots (g-CQDs) from the electrolyte

The CO_2-derived g-CQDs from the reaction system can be separated from the electrolyte comprising MEA, water and $(NH_4)_2SO_4$ by the following step. Firstly, the removal of MEA and water from the solution was achieved by vacuum drying at 150 °C overnight, which results in viscous black liquid. The black liquid was diluted with DI water and then proceeded to the dialysis step using membrane with MWCO of 500 Da and dialyzed time of 12 h with 6 times changing outer DI water to remove $(NH_4)_2SO_4$ salt. As-dialyzed g-CQDs solution was characterized by TEM. The g-CQDs in solid form for other characterizations can be prepared by vacuum drying as-dialyzed g-CQDs solution. It should be noted that, due to their hydrophilic nature, graphitic carbon quantum dots (g-CQDs) are prone to moisture absorption

Characterization

Raman spectra were performed using a Thermos Scientific DXR3 Raman microscope equipped with a 523 nm excitation laser operating at a power of 500 mW and a 100x objective lens. Scanning electron microscope with energy dispersive X-ray analysis (SEM-EDX, Hitachi S-3400N) was employed to examine electrode morphologies and the surface element distribution. UV-Vis-NIR spectra of the electrolyte were obtained using an Agilent Cary 5000 spectrophotometer in the wavelength range of 200-800 nm. The liquid state proton nuclear magnetic resonance (^{1}H NMR) spectra of the electrolyte were obtained using a Fourier transform NMR spectrometer (Bruker AV400 ultra shield, 400 MH) with DMSO-d6 as the solvent. The gaseous products were analyzed by online gas chromatography (Shimadzu GC-2014).

Statistical analysis of Raman, XPS and IR spectra

The baseline correction and the statistical analysis for the whole spectrum of Raman , XPS and IR was attained using Fityk software. The deconvolution of the whole spectrum into single-band profiles proceeded using a Gaussian function so that the integration of intensity and width of single bands is fitted to the whole spectrum.

Calculation of Faradaic efficiency

Due to the presence of various oxygen-containing functional groups on the structure of graphitic carbon quantum dots (g-CQDs), the Faradaic efficiency (FE) was calculated based on the mass of elemental carbon atoms incorporated into the as-synthesized g-CQDs. In this context, the theoretical number of electrons required to reduce CO_2 to a single elemental carbon atom is assumed to be four. Therefore, the Faradaic efficiency can be determined using the following equation.

$$\% \text{ Faradaic efficiency} = \frac{z\,x\,F\,x\,n}{Q}$$

where:

• z = 4, the number of electrons required per carbon atom

• F = 96,485 C mol^{-1}, the Faraday constant

• n is the number of moles of carbon in the product (determined from elemental analysis of g-CQDs)

• Q is the total charge passed during electrolysis, calculated by integrating the current–time (I–t) curve obtained from the potentiostat

This approach provides a reasonable estimation of the electrochemical conversion efficiency of CO_2 to carbon-based products, considering the predominance of elemental carbon atoms in the final g-CQDs framework.

Table for the calculation of % Faradaic efficiency

Types of Electrides	Applied potential (V)	Reaction time (h)	Concentration of g-CQDs (mg/mL)	Total Mole of carbon in g-CQDs (mole)	Total Charge passed during electrolysis (C)	% Faradaic efficiency
$LaCu_{0.67}Si_{1.33}$	-1.00	1.5	0	0	14.82	0
$LaCu_{0.67}Si_{1.33}$	-1.25	1.5	1.60	0.0026	64.41	1557.9
$LaCu_{0.67}Si_{1.33}$	-1.50	1.5	3.12	0.0051	253.3	777.1
$LaCu_{0.67}Si_{1.33}$	-1.75	1.5	4.79	0.0079	390.6	780.6
$LaCu_{0.67}Si_{1.33}$	-2.00	1.5	11.28	0.0185	918.6	777.25
$LaCu_{0.67}Si_{1.33}$	-2.25	1.5	15.20	0.0250	1,102.6	875.1
$LaCu_{0.67}Si_{1.33}$	-1.50	24	157.38	0.2584	19,492.3	511.6
Y_5Si_3	-1.50	1.5	2.66	0.0044	322.5	522.5

Calculation of quantum yield

Measurements of the photoluminescence quantum yield (PLQY) were carried out using a Horiba FluoroMax Plus spectrofluorometer fitted with an integrating sphere (K type). The spectra were recorded in the 420-775 nm range using an excitation wavelength of 400 nm, slit widths of 1 nm for both excitation and emission, and an integration time of 1.0 s.

LCA methodology

To evaluate the environmental impacts of the integrated MEA-based CO_2 capture and electrochemical upgrading to g-CQDs, we conducted a cradle-to-gate life-cycle assessment (LCA) in accordance with ISO 14040 and ISO 14044. The study followed four sequential phases—goal and scope definition; life-cycle inventory analysis; life-cycle impact assessment; and interpretation. The functional unit was 1 t CO_2 captured. The system boundary encompassed gas mixing, feed preparation, ambient-condition electrolysis, , and product purification, with recycling of CO_2 and MEA solvent. Impacts were characterized using ReCiPe 2016 Midpoint (H), and results were determined based on recycling of MEA and chemicals used.

1 .Goal and scope definition

This study's life-cycle assessment (LCA) aims to evaluate the environmental impacts of converting MEA-captured CO_2 into graphitic carbon quantum dots (g-CQDs) via direct electrochemical upgrading and to evaluate any potential of CO_2 utilization via electrolysis pathway. A **cradle-to-gate** system boundary was applied, with g-CQDs defined as the primary product and CO_2 and chemicals recycling accounted for within the system. Accordingly, the functional unit was set to **1 t CO_2 captured and upgraded to g-CQDs** .

2 .Data collection and inventory analysis

The g-CQDs were synthesized through an integrated process combining MEA-based CO_2 capture with electrochemical upgrading. Initially, CO_2 was absorbed into an aqueous MEA solution to generate a CO_2-rich feed, which was subsequently conditioned via gas mixing and feed preparation. The conditioned stream was then subjected to ambient-condition electrolysis, leading to the formation of graphitic carbon quantum dots.

The inventory data for the LCA comprise two categories: background data (e.g., production of MEA and supporting chemicals such as $(NH_4)_2SO_4$; grid electricity, deionized water). Consumption figures for raw materials, distilled/deionized water, chemicals, and energy were derived from laboratory-scale mass and energy balances and normalized to the functional unit of **1 t CO_2 captured**.

Table S1 Life cycle primary inventory for each functional unit (1.00 ton captured)

LCA inventory		Unit	Characterization
Product	g-CQDs	ton	0.4875
Energy consumption		kWh	682
	CO_2	ton	1
	MEA	ton	32.19
	Ammonium sulfate	ton	8.25
	Deionized water	L	109.38

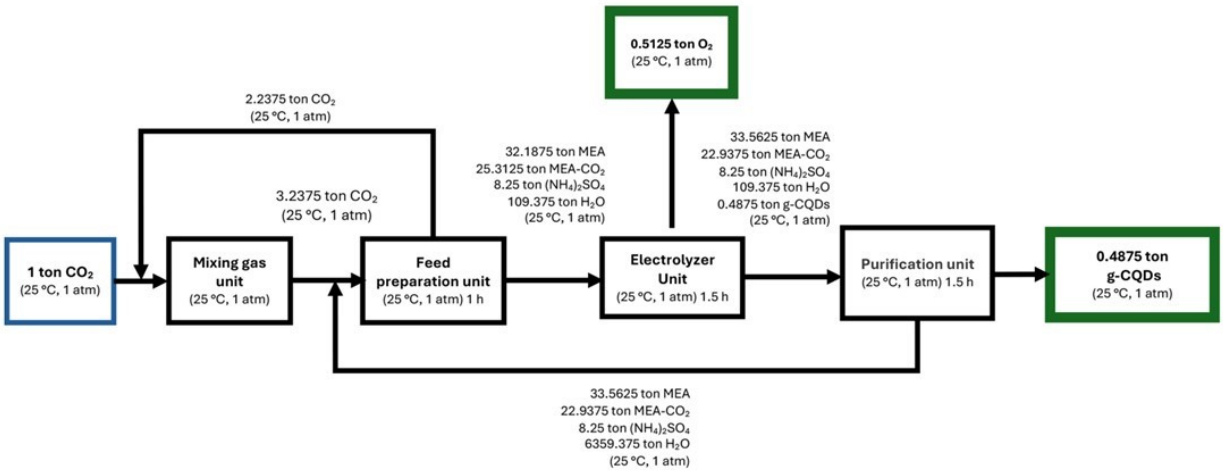

A block flow diagram of the process based on 1 ton CO_2 basis

3 .Life cycle impact assessment

To assess the environmental impacts associated with the proposed chain production system, the ReCiPe 2016 (Hierarchist) V1.09 method was employed. This Life Cycle Impact Assessment (LCIA) methodology was selected for its robust and integrative framework, and was implemented using the SimaPro software version 9.6.0.1. [Pré Consultants, 2019]. Recognized for its harmonization of midpoint indicators, ReCiPe 2016 facilitates a comprehensive evaluation across three principal Areas of Protection (AoP): human health, ecosystems, and natural resources. While the method encompasses 18 midpoint impact

categories[7], six were prioritized in this study due to their significant relevance: global warming (GW), marine eutrophication (ME), terrestrial ecotoxicity (TET), freshwater ecotoxicity (FET), marine ecotoxicity (MET), and human carcinogenic toxicity (HCT).

Supplementary Information

S1

XRD patterns of the synthesized $LaCu_{0.67}Si_{1.33}$ NPs and the calculated band structure and density of states (DOS) of stoichiometric LaCuSi

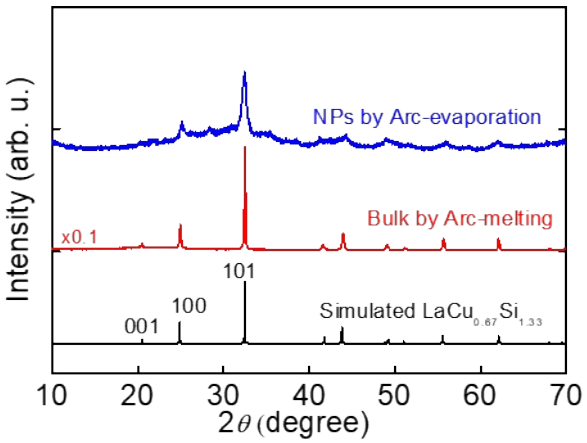

LaCuSi adopts a hexagonal crystal structure composed of Cu–Si honeycomb layers interleaved with La atoms, forming a metal-intercalated honeycomb lattice.

Electronic structure analysis via DFT calculations reveals a prominent interstitial band that crosses the Fermi level, a signature feature of electride behavior. This band does not originate from the Cu 3d orbitals, which are located approximately 4 eV below the Fermi level and exhibit flat-band characteristics, but rather from delocalized electrons occupying interstitial voids, specifically the crystallographic site X (with fractional coordinates 2/3, 1/3, 0). The partial density of states (PDOS) further confirms that this band stems from electron accumulation in the La_3Cu_2 cage and is distinct from the bonding and antibonding states of Cu and Si orbitals. The interstitial electron density at site X manifests as a sharp peak in the DOS near the Fermi level, reinforcing the classification of LaCuSi as an intermetallic electride with intrinsic electron-rich voids that contribute to its metallic conductivity and low work function[8].

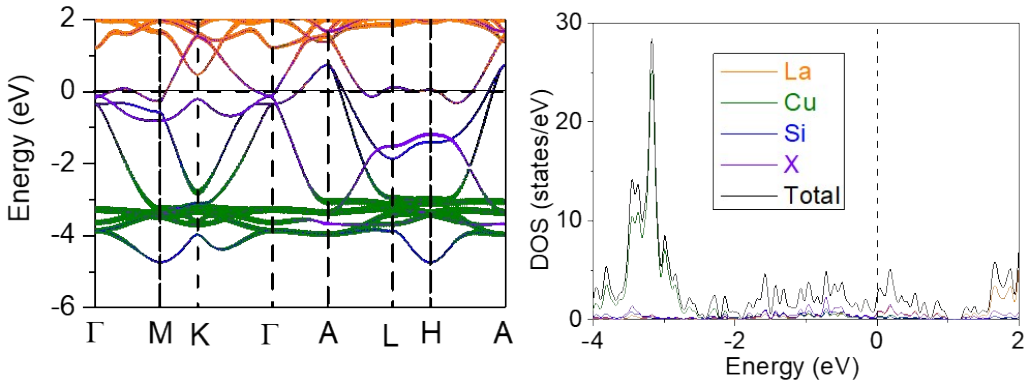

S2

H-Cell membrane-less 50 mL reactor used in this study

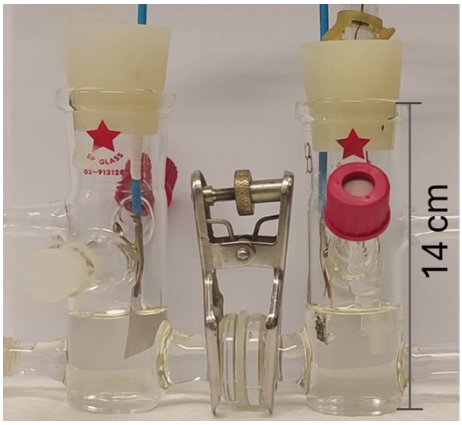

A schematic of the electride NPs coated on Cu foil

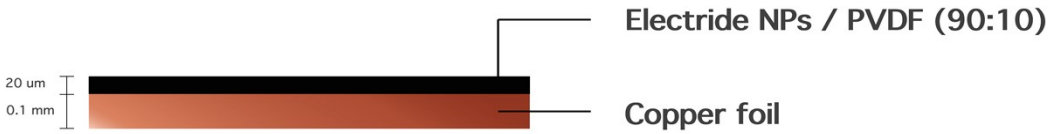

Table S2 The electrochemical conditions in a membrane-less 50 mL H-cell type electrolysis cell

Entry No.	Electride	Substrate	Electrolyte			Applied Potential (V vs. Ag/Ag+)	Reaction time (h)	Temp.
1	$LaCu_{0.67}Si_{1.33}$	Cu foil	30%MEA-CO_2	H_2O	$(NH_4)_2SO_4$	**-1.50**	1.5	25
2	$LaCu_{0.67}Si_{1.33}$	Cu foil	**30%MEA**	H_2O	$(NH_4)_2SO_4$	**-1.50**	1.5	25
3	$LaCu_{0.67}Si_{1.33}$	Cu foil	30%MEA-CO_2	H_2O	$(NH_4)_2SO_4$	**-1.00**	1.5	25
4	$LaCu_{0.67}Si_{1.33}$	Cu foil	30%MEA-CO_2	H_2O	$(NH_4)_2SO_4$	**-1.25**	1.5	25
5	$LaCu_{0.67}Si_{1.33}$	Cu foil	30%MEA-CO_2	H_2O	$(NH_4)_2SO_4$	**-1.75**	1.5	25
6	$LaCu_{0.67}Si_{1.33}$	Cu foil	30%MEA-CO_2	H_2O	$(NH_4)_2SO_4$	**-2.00**	1.5	25
7	$LaCu_{0.67}Si_{1.33}$	Cu foil	30%MEA-CO_2	H_2O	$(NH_4)_2SO_4$	**-2.25**	1.5	25
8	$LaCu_{0.67}Si_{1.33}$	Cu foil	**100%MEA-CO_2**	-	$(NH_4)_2SO_4$	-1.50	1.5	25
9	$LaCu_{0.67}Si_{1.33}$	Cu foil	**100%MEA-CO_2**	**H_2 (g)**	$(NH_4)_2SO_4$	-1.50	1.5	25
10	$LaCu_{0.67}Si_{1.33}$	Cu foil	30%MEA-CO_2	**H_2O + H_2 (g)**	$(NH_4)_2SO_4$	-1.50	1.5	25
11	$LaCu_{0.67}Si_{1.33}$	Cu foil	30%MEA-CO_2 **+ CO_2 (g) flow**	H_2O	$(NH_4)_2SO_4$	-1.50	1.5	25
12	$LaCu_{0.67}Si_{1.33}$	**ITO**	30%MEA-CO_2	H_2O	$(NH_4)_2SO_4$	-1.50	1.5	25
13	$LaCu_{0.67}Si_{1.33}$	**Ni foil**	30%MEA-CO_2	H_2O	$(NH_4)_2SO_4$	-1.50	1.5	25
14	-	**Cu foil**	30%MEA-CO_2	H_2O	$(NH_4)_2SO_4$	-1.50	1.5	25
15	$LaCu_{0.67}Si_{1.33}$	Cu foil	30%MEA-CO_2	H_2O	**$[BMIM][BF_4]$**	-1.50	1.5	25
16	$LaCu_{0.67}Si_{1.33}$	Cu foil	30%MEA-CO_2	H_2O	**$[(CH_3)_3NCH_2CH_2OH]^+Cl^-$**	-1.50	1.5	25
17	$LaCu_{0.67}Si_{1.33}$	Cu foil	30%MEA-CO_2	**D_2O+H_2O (50:50)**	$(NH_4)_2SO_4$	-1.50	1.5	25
18	$LaCu_{0.67}Si_{1.33}$	Cu foil	30%MEA-CO_2	**D_2O (100%)**	$(NH_4)_2SO_4$	-1.50	1.5	25
19	$LaCu_{0.67}Si_{1.33}$	Cu foil	30%MEA-CO_2	H_2O	$(NH_4)_2SO_4$	-1.50	1.5	**60**
20	**Y_5Si_3**	Cu foil	30%MEA-CO_2	H_2O	$(NH_4)_2SO_4$	-1.50	1.5	25
21	$LaCu_{0.67}Si_{1.33}$	Cu foil	30%MEA-CO_2 + CO_2 (g) flow	H_2O	$(NH_4)_2SO_4$	-1.50	**24**	25

S3 [1]H-NMR results of the electrolyte before reaction

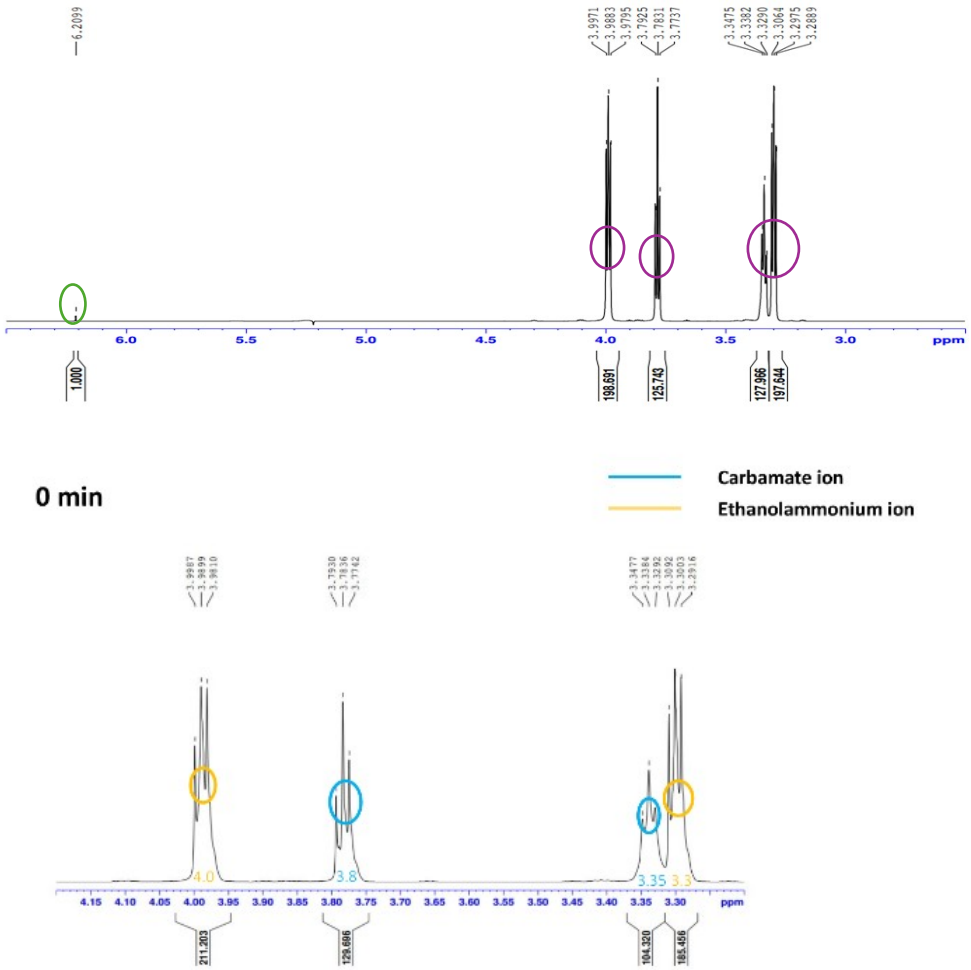

[1]H-NMR results of the electrolyte after reaction at -1.5 V vs. Ag/AgCl for 90 min

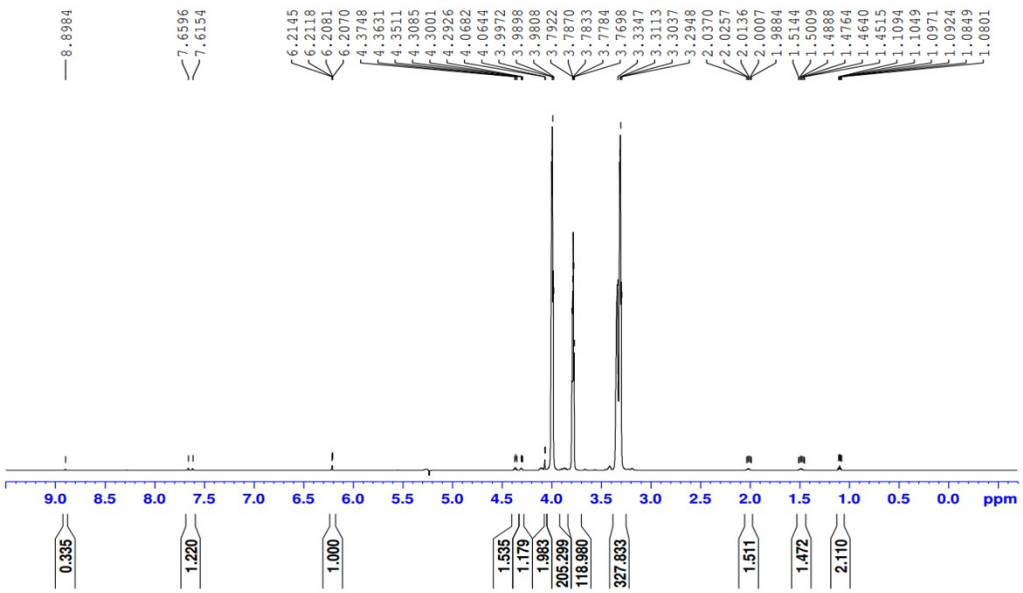

S4 Characterization of as-synthesized g-CQDs

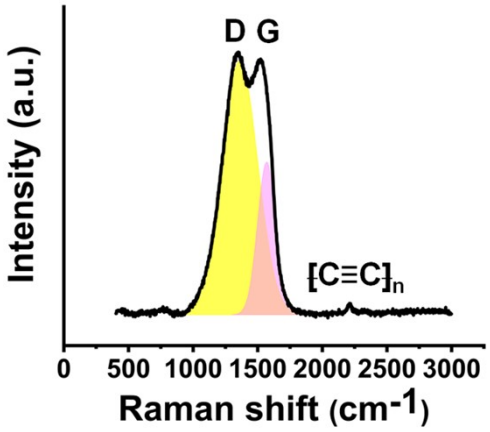

Raman

Raman spectra displayed prominent D (~1348 cm^{-1}) and G (~1515 cm^{-1}) bands, indicating the presence of defect-rich and graphitic carbon frameworks, respectively[9-14]. The I_D/I_G refers to the relative intensity of D to G band from Raman spectra. A higher I_D/I_G indicates a higher degree of disorder or defects in the synthesized CDs[15-17]. The I_D/I_G value of as-synthesized g-CQDs was calculated to be 1.68,demonstrating significant defective structures originated from the presence of various oxygenic functional groups on g-CQDs[18]. In addition, Raman shift at 2210 cm^{-1} can be assigned to sp-carbon chains ($–[C≡C]_n–$)[9-14, 19, 20].

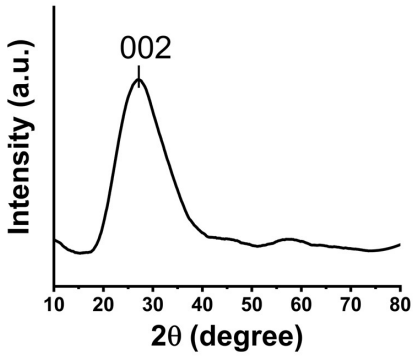

XRD

XRD show prominent (002) graphitic carbon plane at 2θ = 26°, which corresponds to the (002) plane of aromatic layers, where the aromatic ring carbon-reticulated layers are perpendicular to the hexagonal planes through the *c*-axis orientation[21, 22], confirming the graphitic nature of g-CQDs. However, the significant shift and broader peak of (002) reflect the variance of the g-CQDs from the nature graphite structural due to the presence of various oxygenic functional group and nano-meters size of graphitic core in g-CQDs structure[21, 23].

IR

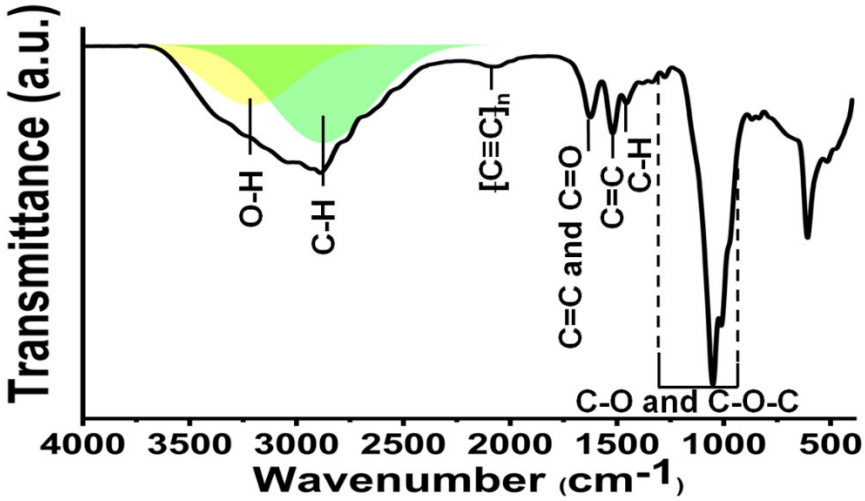

FTIR exhibits the peak related to the graphitic core of g-CQDs at 1520, 1650 cm^{-1}. It should be noted that the peak at 1650 cm^{-1} can be assigned to C=O overlapping with C=C[24]. To elaborate, these peaks are assigned to C=C stretching of aromatic rings of unoxidized graphitic domains[25, 26]. For the oxygenic function groups present on as-synthesized g-CQDs, O-H, C-O/C-O-C are confirmed at 3250 cm^{-1} and 1051, 1012, 1270 cm^{-1}, respectively[27-31]. C-H related bonds are also found at 1456, 2888 cm^{-1} [32, 33]. Surprisingly, sp-carbon chains (–$[C\equiv C]_n$–) was also observed at 2076 cm^{-1}, which is not common with the g-CQDs structure[34, 35].

XPS

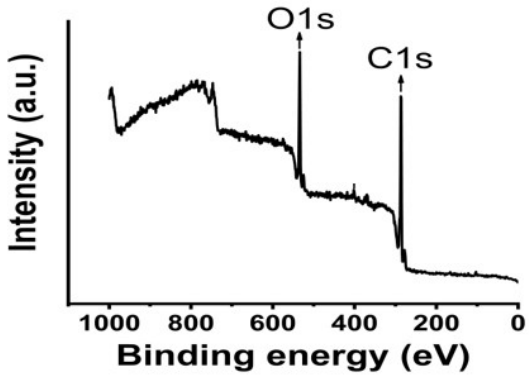

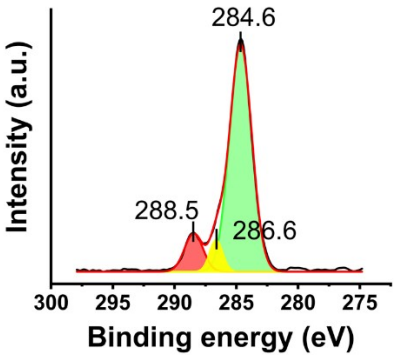

Structure	Binding energy (eV)	% Fraction
C=C/C-C	284.6	81.99
C-OH	286.6	6.59
C=O/O-C=O	288.5	11.41

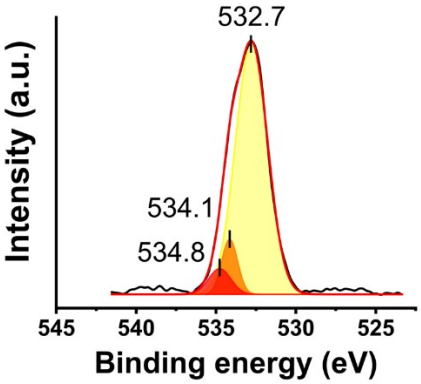

Structure	Binding energy (eV)	% Fraction
C-OH/C-O-C	532.7	84.88
O-C=O	534.1	9.15
C-O/C=O	534.8	5.97

Elemental analysis of XPS demonstrates the presence of carbon atoms and oxygen atoms in as-synthesized g-CQDs with % atomic of 76.5% and 23.5%, respectively. Considering the XPS in the C 1s region, the presence of graphitic C–C/C=C, C–OH and C=O/O–C=O is observed at 284.6, 286.6, and 288.5 eV, respectively[36-38]. The portion of graphitic C–C/C=C takes an account of > 80 % in the structure, showing high ratio of graphitic core. While in the O 1s region, C–OH/C–O–C species have been observed at 532.7 eV, O–C=O at 534.1 eV and C–O/C=O at 534.8 eV[39, 40].

S5 Calibration curve of the UV–vis absorbance intensity and the concentration of as-purified g-CQDs dispersed in deionized water

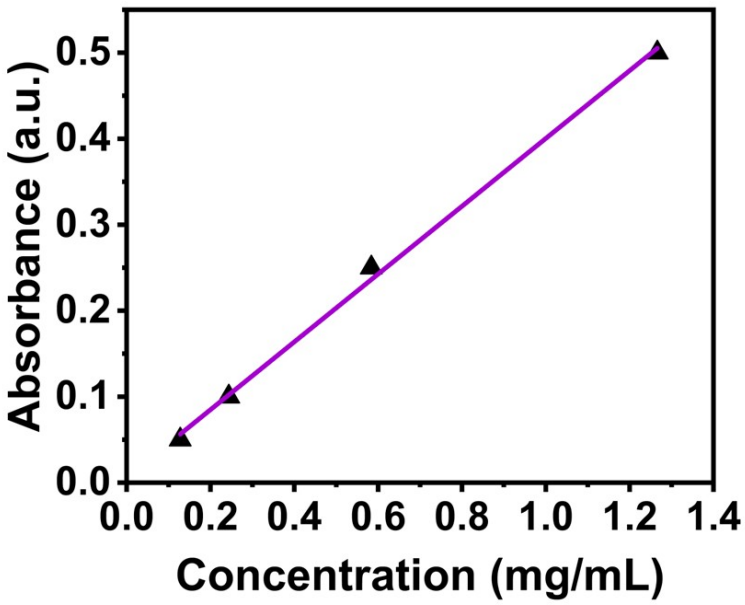

The UV–vis calibration curve was constructed by plotting the absorbance intensity of as-purified g-CQDs dispersed in deionized water against their concentration, using the characteristic graphitic-core absorption peak in the 280–300 nm range. This calibration was subsequently used to quantify the concentration of as-synthesized g-CQDs in the electrolyte, thereby avoiding the inaccuracies associated with gravimetric analysis, as g-CQDs readily absorb moisture due to their hydrophilic surface chemistry.

S6 GC and ^{1}H-NMR analysis of the electrochemical reaction using $LaCu_{0.67}Si_{1.33}$@Cu foil electrodes at -1.5 V vs. Ag/AgCl for 90 min

GC results

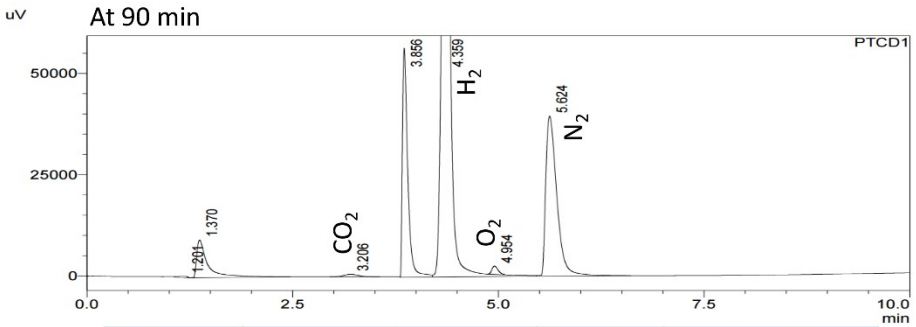

Peak Name	Ret. Time	Area	Height	Rate (μmol/min)
CO_2	3.206	7353	605	6.58E-10
H_2	4.359	1092922	174380	2.53E-08
O_2	4.954	11104	2091	
N_2	5.624	368969	39471	

^{1}H-NMR results of the electrolyte during the electrochemical reaction using $LaCu_{0.67}Si_{1.33}$@Cu foil electrodes at -1.5 V vs. Ag/AgCl for 1, 5, 10, 30, 60, and 90 min

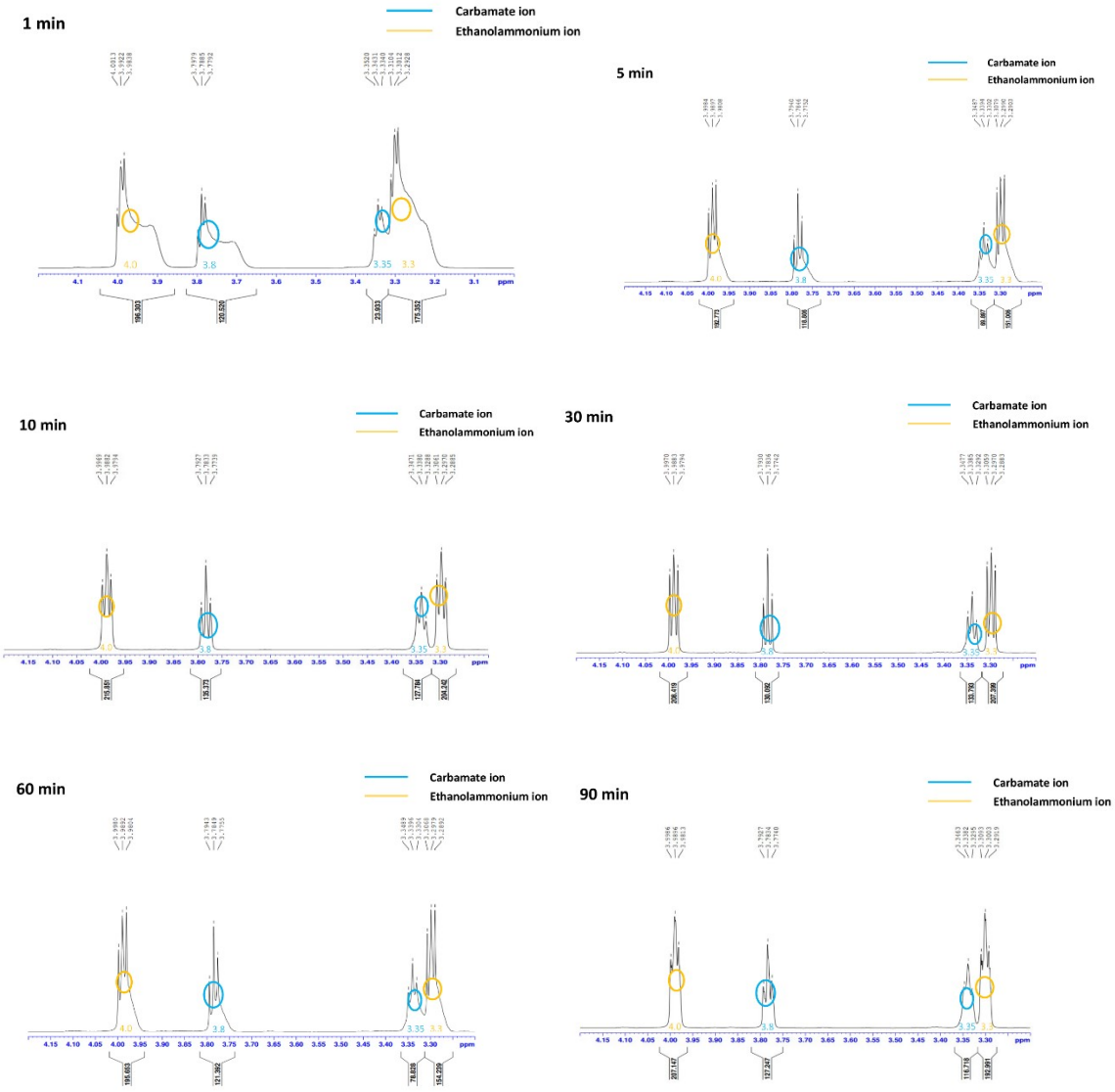

CO_2 conversion at -1.5 V and 90 mins from ^{1}H-NMR results

Chemical	Area	Micro Mole
Maleic acid	1	-
Carbamate ions (before)	125.74	77122.4
Carbamate ions (after)	114.0	69917.6

% Conversion = 9.34%

S7 ^{1}H-NMR results of the electrolyte during the electrochemical reaction using $LaCu_{0.67}Si_{1.33}$@Cu foil electrodes at -1.5 V vs. Ag/AgCl for 90 min with 30%MEA-CO_2 and continuous CO_2 flow during the reaction

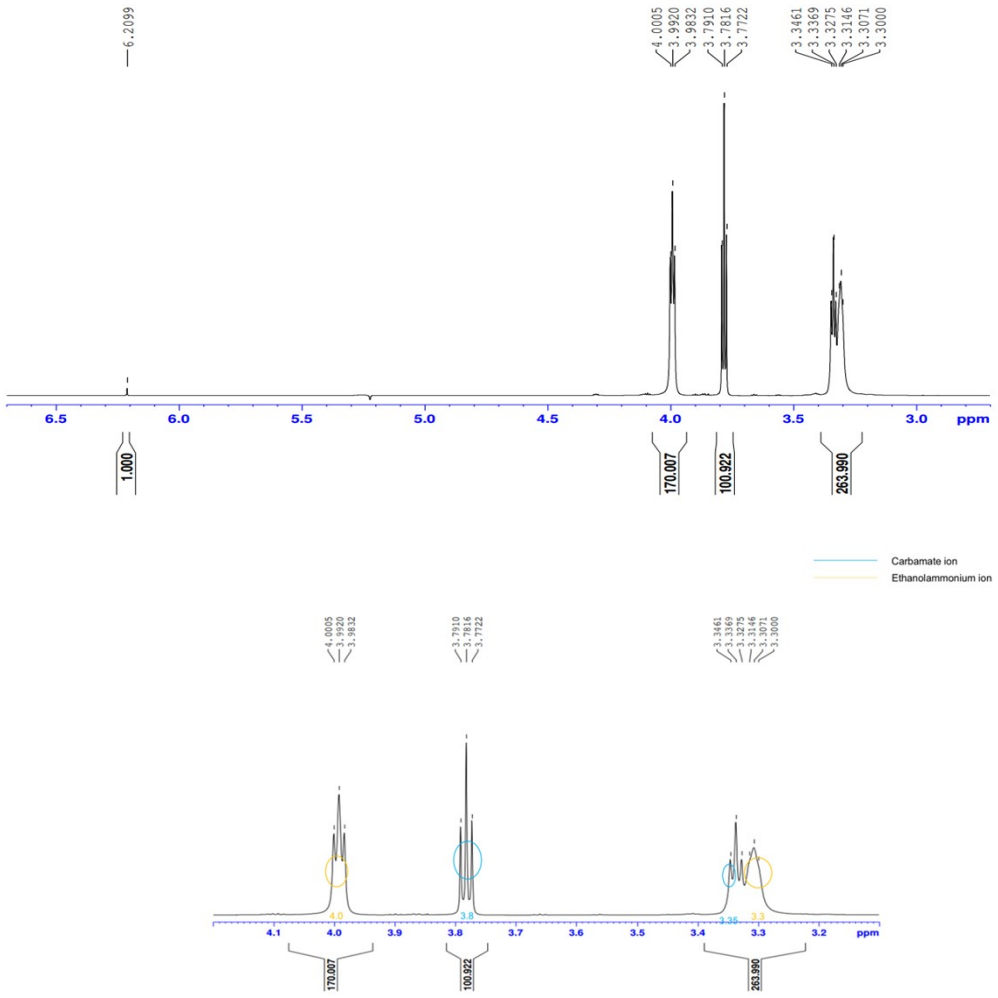

CO_2 conversion at -1.5 V and 90 min from ^{1}H-NMR results

Chemical	Area	Micro Mole
Maleic acid	1	-
Carbamate ions (before)	125.74	77122.4
Carbamate ions (after)	100.92	61898.8

% Conversion = 19.7%

S8 Experimental results of the electrochemical reaction using $LaCu_{0.67}Si_{1.33}$@Cu foil electrodes with gaseous CO_2 in aqueous solution containing 0.4 M $(NH_4)_2SO_4$ at -1.5 V vs. Ag/AgCl for 90 min

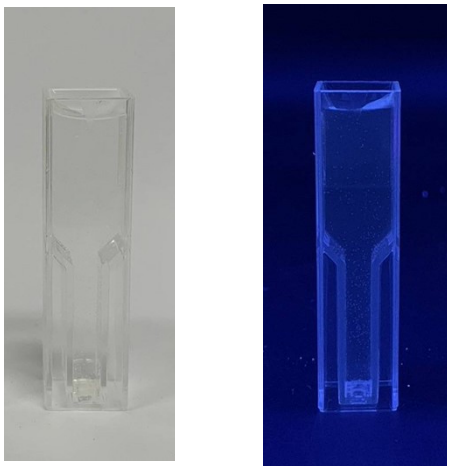

S9 A proposed chemical reaction pathway for radical-mediated dehydration and C–C coupling of hydrogenated-CO_2 intermediates

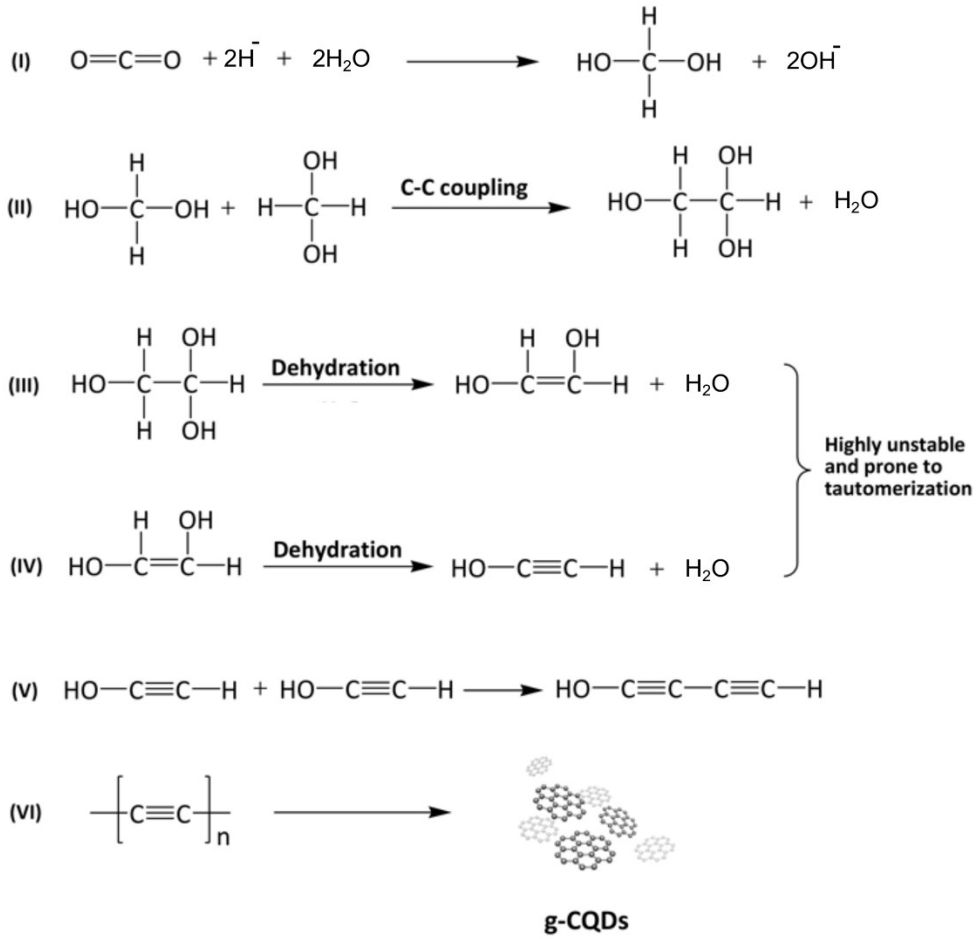

A proposed chemical pathway for g-CQD formation is presented in **Fig. S9**. Since no liquid products were detected in ^{1}H NMR results at various reaction time points (e.g., 1, 5, 10, 30, 60, 90 min), the traditional hydride transfer pathway is unlikely to support g-CQD formation, as it typically proceeds via a stepwise mechanism yielding hydrogenated products such as HCOOH or CH_3OH[41-43]. The only plausible scenario involves hydride transfer occurring simultaneously across the surface to react with regenerative CO_2 molecules. This mechanism becomes feasible under conditions where synchronized, field-driven electron tunneling-induced hydride transfer takes place. Supported by our experimental findings and prior studies showing the conversion of concentrated CO_2 and hydrides into graphitic carbon under ambient conditions[44-46], as well as established bottom-up mechanisms for CQD formation via C–C coupling through dehydration pathways[47-54].

The reaction likely begins with the formation of hydrogenated intermediates containing

both C–H and C–OH functional groups, facilitated by the interaction of CO_2 and hydride species in aqueous media. This is supported by **IR and XPS** characterization of as-synthesized g-CQDs (**Fig. S4**), which show prominent signals corresponding to C–H and C–OH bonds in the as-synthesized g-CQDs. These hydrogenated intermediates can undergo intramolecular coupling followed by dehydration to form hydroxylated acetylenes. The enol/ynol-type intermediates generated during the reaction are inherently unstable and readily undergo keto–enol tautomerization, yielding thermodynamically more stable carbonyl species[55]. However, these carbonyl species are unlikely to directly convert into g-CQDs under ambient conditions, suggesting that the formation of g-CQDs proceeds via a rapid, concerted pathway, likely involving the simultaneous coupling and dehydration of reactive intermediates before tautomerization can occur.

Notably, the formation of unsaturated C_2 intermediates from hydroxyl precursors under mild conditions has also been reported in recent studies using plasmonic Ag nanoparticles (Ag NPs) to catalyze the ambient-temperature transformation of ethanol to graphene oxide. Raman spectra in those studies confirmed the presence of linear acetylenic carbon or long-chain poly-yne species[56]. Owing to their intrinsic instability, such linear acetylenic carbon structures have been shown to spontaneously reorganize into graphitic carbon even at room temperature[57]. In our system, trace amounts of linear acetylenic carbon were detected via **IR and Raman spectroscopy** (**Fig. S4**), suggesting that these species serve as key intermediates.

The concurrent formation of hydroxyl acetylenes likely facilitates intermolecular dehydration, leading to polyyne formation, which can subsequently undergo cyclization or condensation to yield g-CQDs. Additionally, the presence of a highly localized electric field is hypothesized to promote the homolytic cleavage of polar bonds such as C–OH, generating carbon-centered and hydroxyl radicals. These reactive species may then initiate chain reactions, continuously producing carbon radicals that drive C–C bond formation via a radical-mediated polymerization mechanism.

To clarify the $\%FE_{CQDs}$ values exceeding 100% observed in this work, we attribute this to the non-classical, field-driven, and charge-recycling nature of the g-CQDs-mediated CO_2 conversion process. As a matter of fact, %FE values exceeding 100% have been reported in various electrochemical and field-driven systems, where the classical assumption of a strict one-to-one correspondence between externally supplied electrons and product formation no longer applies. A recent comprehensive review by W. Ge et al.[58] has systematically summarized electrochemical systems exhibiting %FE > 100% and categorized the underlying mechanisms into several classes, including non-equilibrium electron transport. In such

systems, strong potential gradients, localized electric fields, and charge accumulation give rise to non-classical behavior, whereby a single externally injected electron can sequentially participate in multiple interfacial chemical events before being registered as net charge in the external circuit. In addition, %FE > 100% is commonly observed in plasma-driven solution electrolysis systems[59, 60], where non-Faradaic pathways contribute significantly to product formation through radical-mediated reactions[4]. Localized electric fields are widely recognized as the key factor leading to %FE values exceeding 100%. Such fields not only stabilize radical intermediates and transition states[61, 62], but can also induce bond dissociation through polarization effects[63, 64], thereby enabling chemical transformations without direct electron transfer from the external circuit. Notably, intense localized electric fields generated at plasmonic metal nanoparticles have been shown to activate CO or CO_2 molecules and promote C–O bond cleavage even in the absence of additional chemical reagents. These processes are generally attributed to electric-field-driven and hot-carrier-mediated bond dissociation mechanisms[65, 66].

In our study, the strong localized electric field within the electride nanocages can simultaneously induce water dissociation into $H^{\cdot}$ and $OH^{\cdot}$ radicals[67, 68]. Under such intense fields, hydrogen radicals become strongly polarized and can transiently adopt hydride-like character[67, 69]. These field-polarized hydrogen species, together with electric field-induced polarization and weakening of C–O bonds in CO_2, facilitate carbon formation without requiring direct electron transfer from the external circuit. Once g-CQDs are formed, non-Faradaic pathways are significantly amplified. The cathodic Faradaic reaction at the electrode/electrolyte interface can be expressed as $CO_2 + 2H^- \rightarrow C + 2OH^-$, where electrons supplied from the external circuit are transferred in the form of hydride equivalents and ultimately appear as hydroxide ions associated with the carbon product. Crucially, hydrogen radicals generated by field-induced water dissociation can react with hydroxide ions to regenerate water and produce solvated electrons[70, 71] ($H^{\bullet} + OH^- \rightarrow H_2O + e^-$). The released electrons subsequently relocalize within the g-CQDs network, resulting in negatively charged g-CQDs that sustain persistent localized electric fields due to electron confinement within graphitic domains. Although the localized electric field on g-CQDs is weaker than that inside electride nanocages, g-CQDs can act as nucleation seeds to promote further growth of g-CQDs from CO_2[72]. The localized electric fields associated with negatively charged g-CQDs further induce water dissociation and C–O bond cleavage, thereby enabling additional g-CQD formation without direct electron transfer from the external circuit. The formation of negatively charged g-CQDs is experimentally supported by their electrophoretic migration from anode to

cathode, confirming their net negative charge (see **Supplementary video**).

At steady state, hydroxide ions and hydrogen radicals generated at the electride/electrolyte interface engage in continuous charge-relocalization cycles. Electrons from the electride are dynamically redistributed into the g-CQDs network via radical-mediated interactions, while electrons confined within g-CQDs can simultaneously transfer to hydroxyl radicals to regenerate hydroxide ions. The self-sustained dynamic equilibrium preserves a persistently negatively charged g-CQD network without net electron generation. Such charge-recycling behavior is expected to enhance hydroxide-mediated ionic transport, lower the effective electrolyte resistance, and drive the monotonic increase in current density observed experimentally over ~1.5 h. Consequently, multiple carbon-forming events can occur per net electron recorded in the external circuit. When Faradaic efficiency is calculated using the conventional charge-based definition, an apparent %FE > 100% naturally arises. Importantly, this phenomenon does not violate charge conservation; rather, it reflects the fundamentally non-classical, field-driven, and charge-recycling nature of the g-CQDs-mediated CO_2 conversion process.

S10 F–N Model Calculation

$$\mathrm{I} = \frac{Aq^3V^2}{8\pi h\phi_B d^2 m^*} \frac{m}{exp\left(-\frac{8\pi d(2m^*)^{1/2}\phi_B^{3/2}}{3hq} \frac{}{V}\right)} \quad \textbf{(1)}$$

Where:

q is the elementary charge of the electron (C) = 1.602×10^{-19} C

A is the effective tunneling area (m^2)

h is Planck's constant (J·s) = 6.625×10^{-34} J·s

V is the applied voltage (V)

d is the tunneling barrier width (m) = 0.5×10^{-9} m

ϕ_B is the tunneling barrier height (eV)

m is the mass of the electron = 9.109×10^{-31} kg

m^* is the effective mass of the electron = 9.109×10^{-31} kg (assume that anionic electrons in electride behave as free electrons)

By taking the natural logarithm of both sides of Equation **(1)**, we obtain Equation **(2)**:

$$ln(\mathrm{I}/V^2) = -\frac{8\pi d(2m^*)^{1/2}\phi_B^{3/2}}{3hq}\frac{1}{V} + \ln\frac{Amq^3}{8\pi m^* hd^2\phi_B} \quad \textbf{(2)}$$

By plotting $\ln(I/V^2)$ as the y-axis and 1/V as the x-axis, the tunneling barrier height Φ_B can be extracted from the slope of the linear region, as described in Equation **(3)**:

$$\text{Slope} = -\frac{8\pi d(2m^*)^{1/2}\phi_B^{3/2}}{3hq} \quad \textbf{(3)}$$

Substituting all fundamental constants and unit conversion factors into Equation **(3)**, we simplify the expression for Φ_B (in eV), in which slope must be in the unit of V as:

Slope from the experimental set I = -6.174 V

Therefore, $\phi_B\,(eV) = -\frac{Slope^{2/3}}{2.268} = -\frac{-6.174^{2/3}}{2.268}$ = 1.483 eV

S11 Fowler–Nordheim (F–N) tunneling model fitting using another experimental dataset

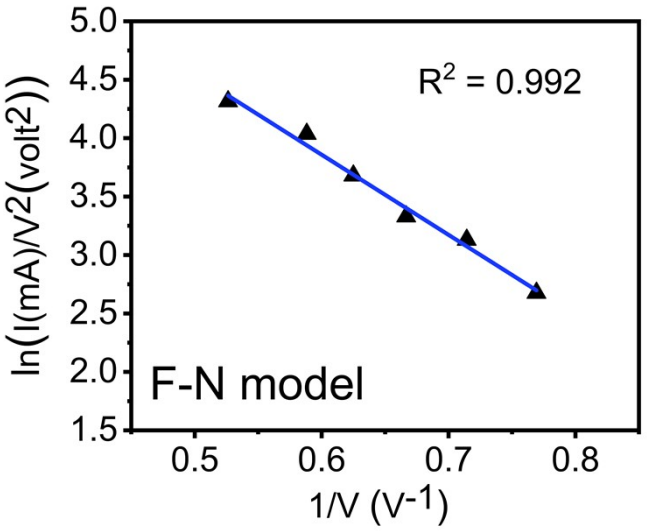

Slope from the experimental set II = -6.174 V

Therefore, $\phi_B\,(eV) = -\frac{Slope^{2/3}}{2.268} = -\frac{-6.742^{2/3}}{2.268}$ = 1.574 eV

S12 Structure and Performance of Y_5Si_3 electride on Cu foil in the electrochemical conversion of 30% MEA-CO_2 at -1.5 V vs. Ag/AgCl

According to the literature[73], Y_5Si_3 electride is a chemically robust intermetallic electride, crystallizing in the Mn_5Si_3-type structure. It stabilizes ~0.79 anionic electrons per formula unit within quasi-one-dimensional interstitial channels along the c-axis. These anionic electrons exhibit strong hybridization with Y 4d orbitals, imparting high chemical stability and exceptional electron-donating properties.

The concept of electron tunneling induced hydride transfer for conversion of CO_2 into g-CQDs was further validated using Y_5Si_3 electride. However, the $\%FE_{CQDs}$ of Y_5Si_3 (523%) was noticeably lower than that of $LaCu_{0.67}Si_{1.33}$ ($\%FE_{CQDs} \approx 777$ %). This difference may stem from the intrinsic void electron density within each electride. In $LaCu_{0.67}Si_{1.33}$, the densely packed interstitial electrons generate strong localized electric fields, effectively facilitating coherent electron tunneling to drive hydride transfer. In contrast, Y_5Si_3 features a distinct structure framework with lower inherent electron density within its voids, requiring greater external electron injection to attain comparable field strength. Nevertheless, Y_5Si_3 ultimately achieves g-CQDs yields comparable to those of $LaCu_{0.67}Si_{1.33}$. These findings suggest the role of void electron density in enabling tunneling catalysis, offering a key parameter for future investigation.

Current Density **UV-Vis results (**diluted 10x)

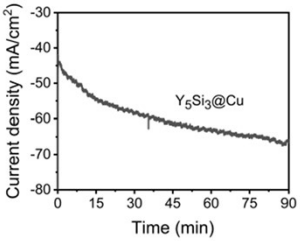

% FE_{CQDs} = 523 %

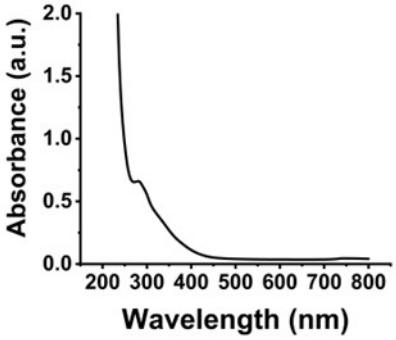

S13 the electrochemical conversion of 30% MEA-CO_2 in 0.4 M $(NH_4)_2SO_4$ at -1.5 V vs. Ag/AgCl using $LaCu_{0.67}Si_{1.33}$@Cu foil electrodes at a constant current **0.053 A**

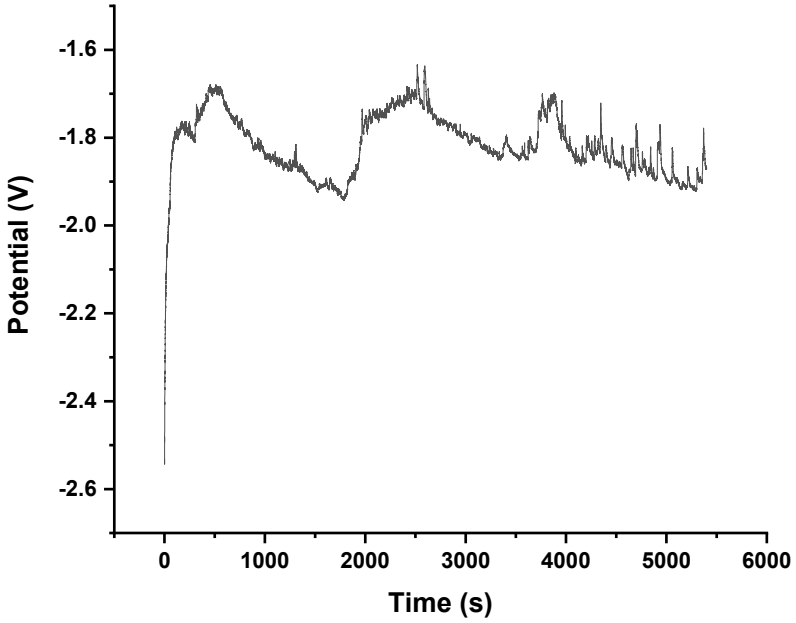

Supplementary Table S3 Energy consumption of CO_2-to-solid carbon processes

Process	State of CO_2	Products	Products Yield	Temp.	Pressure	Energy Source	Energy per kg products	Regeneration of active species	Carbon deposit on catalytic sites	Ref.
Electrochemical process with tunneling electron transfer (intermetallic electride cathode)	MEA-CO_2 (in H_2O)	g-CQDs	6,133 μmol/h	25 °C	1 bar	Electrical energy	1.90 KWh/kg C	Yes	No	This study
Electrochemical process with classical electron transfer (liquid metal cathode)	CO_2	Amorphous solid carbon	52.4* μmol/h	25 °C	1 bar	Electrical energy	47.71* KWh/kg C	Yes	Partly***	Ref[74]
Molten Salt Electrolysis	CO_2	Graphite and CNTs	N/A	750 °C	1 bar	Electrical energy	44.06 – 129.53 Kwh/kgC	Yes	Yes	Ref[75]
Thermochemical process	CO_2	Solid Carbon	319 μmol/h	200 °C	1 bar	-	n/a	No	Partly***	Ref[76]
Tandem electrochemical and thermochemical processes	CO_2 (for electrolytic production of CO + H_2)	Carbon nanofiber	2.5 g Carbon/g cat./h	25 °C (for electrolysis)	1 bar	Electrical energy	162 KWh/kgC	No	Yes	Ref[77]

	$CO + H_2$ (for carbon nanofibers formation)			370 – 450 °C (for thermochemical)						
Tribo-electrochemical process	MEA-CO_2 (in DMF)	Carbonaceous solid producrs	30,000 µmol/h	40 °C	1 bar	Mechanical energy	0.843 KWh/kgC	Partly**	Partly***	Ref[78]
DBD Plasma process	CO_2	Nanocarbon	709.92* µmol/h	25 °C	1 bar	Electrical energy	1185.56* KWh/kgC	No	Partly***	Ref[79]

*Reported energy values were derived based on accessible data in the reference, **The regeneration process requires direct contact of liquid metal oxide and Ag, ***Growth on catalytic sites but automatically separated by liquid metal nature

Supplementary Table S4 Low-energy pathways for the formation of solid carbon through reactions between CO_2 and reactive hydrogen species

System	State of CO_2	Catalytic sites	Hydrogen sources	Reaction Conditions		Carbon Products	Highly Localized CO_2 concentration	Highly Localized hydrogen species	Oxygen removal pathway	Ref.
Electrochemical	MEA-CO_2	H-passivated $LaCu_{0.67}Si_{1.33}$ intermetallic electride	H^- from H_2O	-1.5 V (vs. Ag/AgCl)	25 °C, 1 bar	g-CQDs aqueous electrolyte	Yes	Yes	OH^- with O_2 as final products	This work
Electrochemical	1 bar CO_2	Negatively Charged metal NPs	H_2O	-1.1 to -1.6 V (vs Ag/AgCl)	25 °C, 1 bar	Nanocrystalline solid carbon on the cathodes	Yes	Yes	OH^- with O_2 as final products	[80]
Electrochemical	100 bar CO_2	Stainless Steel	H^+ from CH_3OH	3 to 10 V (cell voltage)	50 °C, 100 bar	Carbon film on the cathode	Yes	Yes	H_2O	[81]
Mechanochemical	20 bar CO_2	Direct Chemical reaction	NaH	Milling rate = 500 rpm	25 °C, 20 bar CO_2	Carbon materials with various morphologies	Yes	Yes	Na_2O/ Na_2CO_3	[46]
Thermochemical	5-30 bar CO_2	Direct Chemical reaction	LiH		25 °C, 5-30 bar	Nanocarbon with various morphologies	Yes	Yes	O_2, Li_2O/Li_2CO_3	[82]

Thermochemical	35 bar CO_2	Direct Chemical reaction	$LiAlH_4$		126 °C, 75 bar	Graphite	Yes	Yes	$LiAlO_2$, Li_2CO_3	[44]
Calcination	$CaCO_3$	Direct Chemical reaction	$NaBH_4$	Template Structure of Calcium $CaCO_3$/ $NaBH_4$	Calcined at 500 °C for 2 h followed by 700 °C for 2 h	Highly interconnected $CaCO_3$/Carbon Composite	Yes	Yes	CaO	[83]
Calcination	$NaHCO_3$	Direct Chemical reaction	$NaBH_4$	Mixed powder $NaBH_4$/$NaHCO_3$	Calcined at 600 °C for 2 h	Porous Carbon Sheet	Yes	Yes	Na_2O	[84]

Table S5 The environmental indicators and overall impacts of g-CQDs synthesized from CO_2.

Impact category	Unit	Characterization	Normalization
Global warming potential (GWP)	kg CO_2 eq	523.30	0.0654
Stratospheric ozone depletion potential (ODP)	kg CFC11 eq	0.00014	0.0023
Ionizing radiation potential (IRP)	kBq Co-60 eq	1.224	0.0025
Ozone formation potential for Human health (HOFP)	kg NO_x eq	0.813	0.0395
Ozone formation potential for Terrestrial ecosystems (EOFP)	kg NO_x eq	0.843	0.0474
Fine particulate matter formation potential (PMFP)	kg PM2.5 eq	0.494	0.0193
Terrestrial acidification potential (TAP)	kg SO_2 eq	1.286	0.0314
Freshwater eutrophication potential (FEP)	kg P eq	0.401	0.6171
Marine eutrophication potential (MEP)	kg N eq	0.032	0.0069
Terrestrial ecotoxicity potential (TETP)	kg 1,4-DCB	1487.832	0.0979
Freshwater ecotoxicity potential (FETP)	kg 1,4-DCB	33.902	1.3459
Marine ecotoxicity potential (METP)	kg 1,4-DCB	44.466	1.0227
Human carcinogenic toxicity potential (HTPc)	kg 1,4-DCB	48.049	4.6655
Human non-carcinogenic toxicity potential (HTPnc)	kg 1,4-DCB	644.377	0.0206
Land use potential (LUP)	m2a crop eq	4.009	0.0006
Mineral resource scarcity potential (MRSP)	kg Cu eq	0.825	6.8693
Fossil resource scarcity potential (FRSP)	kg oil eq	155.185	0.1583
Water consumption potential (WCP)	m^3	1.963	0.0074

The LCA results are given in **Table S5**. The global warming potential (GWP) assessment indicates net greenhouse gas emissions of approximately 0.52 t CO_2-eq. The integration of CO_2 capture and utilization can partially offset these emissions, yielding a net value of less than 1 t CO_2-eq per t CO_2, thereby underscoring the system's significant potential to mitigate climate change. Furthermore, both CO_2 and MEA can be recycled within the production chain, reducing dependence on fresh raw materials and minimizing waste generation, and thereby enhancing resource efficiency. It should be noted that g-CQDs themselves can contribute to CO_2 mitigating through integration into CCUS (CO_2 Capture, Utilization, and Storage) technologies. In the capture stage, g-CQDs have been employed as adsorbents in CO_2 capture owing to their abundant surface functional groups and strong affinity toward CO_2 molecules[80, 81]. In the utilization stage, numerous studies have highlighted their catalytic potential for CO_2 conversion into fuels and other value-added products, including applications as electrocatalysts[82, 83] and photocatalysts[82, 84]. Due to their solid-state nature under ambient conditions, g-CQDs also offer an effective storage forms CO_2, avoiding leakage issues associated with liquid or gaseous products[74]. Moreover, g-CQDs are not only biocompatible[85, 86], but also capable of improving soil health[87], making them suitable for storage in soil without adverse impacts on the soil environment. Beyond CCUS, g-CQDs have also been applied in the renewable energy sector, including energy storage devices such as Li-ion batteries[88, 89] and green energy harvesting systems such as solar cells[90, 91]. In addition, incorporating small amounts of g-CQDs into cement composites has been shown to significantly enhance mechanical strength[92, 93], thereby reducing cement demand in this highly CO_2-intensive emission industry[94]. Thus, beyond mitigating emissions through their synthesis pathway, the downstream applications of g-CQDs offer substantial additional climate benefits. To further enhance sustainability, targeted strategies are required to mitigate carcinogenic impacts, which represent the primary environmental concern of this process. Overall, the LCA indicates that the system operates as a net negative-CO_2 technology even when powered by conventional energy sources, while also exhibiting comparatively favorable environmental impacts.

References

1. Y. Lu, J. Li, T.-N. Ye, Y. Kobayashi, M. Sasase, M. Kitano and H. Hosono, *ACS Catalysis*, 2018, **8**, 11054-11058.
2. G. Kresse and J. Furthmüller, *Physical Review B*, 1996, **54**, 11169-11186.
3. J. P. Perdew, K. Burke and M. Ernzerhof, *Physical Review Letters*, 1996, **77**, 3865-3868.
4. G. Kresse and D. Joubert, *Physical Review B*, 1999, **59**, 1758-1775.
5. H. J. Monkhorst and J. D. Pack, *Physical Review B*, 1976, **13**, 5188-5192.
6. G. Lee, Y. C. Li, J. Y. Kim, T. Peng, D. H. Nam, A. Sedighian Rasouli, F. Li, M. Luo, A. H. Ip, Y. C. Joo and E. H. Sargent, *Nature Energy*, 2021, **6**, 46-53.
7. M. A. J. Huijbregts, Z. J. N. Steinmann, P. M. F. Elshout, G. Stam, F. Verones, M. Vieira, M. Zijp, A. Hollander and R. van Zelm, *The International Journal of Life Cycle Assessment*, 2017, **22**, 138-147.
8. T. N. Ye, Y. Lu, J. Li, T. Nakao, H. Yang, T. Tada, M. Kitano and H. Hosono, *Journal of the American Chemical Society*, 2017, **139**, 17089-17097.
9. H. Pang, X. Wang, G. Zhang, H. Chen, G. Lv and S. Yang, *Applied Surface Science*, 2010, **256**, 6403-6407.
10. Y. Liu, Y. Hu and J. Zhang, *Journal of Physical Chemistry C*, 2014, **118**, 8993-8998.
11. Q. Xu, X. Lin, L. Gan, G. Owens and Z. Chen, *Journal of Colloid and Interface Science*, 2022, **605**, 881-887.
12. J. Hong, M. K. Park, E. J. Lee, D. Lee, D. S. Hwang and S. Ryu, *Scientific Reports*, 2013, **3**, 2700.
13. A. C. Ferrari, *Solid State Communications*, 2007, **143**, 47-57.
14. V. A. Yolshina, L. A. Yolshina, V. A. Elterman, E. G. Vovkotrub, A. A. Shatunova, V. I. Pryakhina, N. A. Khlebnikov and N. V. Tarakina, *Materials and Design*, 2017, **135**, 343-352.
15. W. D. Yang, J. X. Wang, Y. T. Wu, H. S. Chang and H. H. Ko, *Materials*, 2022, **15**.
16. F. Mori, M. Kubouchi and Y. Arao, *Journal of Materials Science*, 2018, **53**, 12807-12815.
17. A. Samsul Kamal, N. H. Jabarullah and R. Othman, 2020.
18. R. Rabeya, S. Mahalingam, A. Manap, M. Satgunam, M. Akhtaruzzaman and C. H. Chia, *International Journal of Quantum Chemistry*, 2022, **122**, e26900.
19. E. O'Bannon, G. Xia, F. Shi, R. Wirth, A. King and L. Dobrzhinetskaya, *Diamond and Related Materials*, 2020, **108**, 107876.
20. B. Pan, J. Xiao, J. Li, P. Liu, C. Wang and G. Yang, *Science Advances*, 2015, **1**.
21. M. Salvatore, G. Carotenuto, S. De Nicola, C. Camerlingo, V. Ambrogi and C. Carfagna, *Nanoscale Research Letters*, 2017, **12**.
22. M. A. Ahmad Farid, J. Lease, A. L. T. Zheng, T. Tsubota and Y. Andou, *ACS Sustainable Resource Management*, 2024, **1**, 97-113.

23. D. Ozyurt, M. A. Kobaisi, R. K. Hocking and B. Fox, *Carbon Trends*, 2023, **12**, 100276.
24. X. Guo, Y. Guo and X. Chen, *Journal*, 2024, **25**.
25. T. Emiru and D. Ayele, *Egyptian Journal of Basic and Applied Sciences*, 2016, **4**.
26. X. Chen, F. Yan, J. Li and X. Gong, *JACS Au*, 2025, **5**, 1350-1358.
27. D. Nugroho, W.-C. Oh, S. Chanthai and R. Benchawattananon, *Journal*, 2022, **12**.
28. A. Shaikh, M. Tamboli, R. Patil, A. Bhan, J. Ambekar and B. Kale, *Journal of nanoscience and nanotechnology*, 2019, **19**, 2339-2345.
29. H. Nie, M. Li, Q. Li, S. Liang, Y. Tan, L. Sheng, W. Shi and S. Zhang, *Chemistry of Materials*, 2014, **26**, 3104–3112.
30. J. Zhao, J. Wang, L. Zeng, S. Zhou and X. Yang, *Chinese Journal of Chemistry*, 2023, **41**, 3677-3683.
31. J. Wang, Z. Zhou, Q. Li, T. Zhang and Y. Fu, *Spectrochimica Acta Part A: Molecular and Biomolecular Spectroscopy*, 2024, **315**, 124285.
32. J. Ren, F. Weber, F. Weigert, Y. Wang, S. Choudhury, J. Xiao, I. Lauermann, U. Resch-Genger, A. Bande and T. Petit, *Nanoscale*, 2019, **11**, 2056-2064.
33. A. Filopoulou, S. Vlachou and S. C. Boyatzis, *Journal*, 2021, **26**.
34. L. D. Movsisyan, M. D. Peeks, G. M. Greetham, M. Towrie, A. L. Thompson, A. W. Parker and H. L. Anderson, *Journal of the American Chemical Society*, 2014, **136**, 17996-18008.
35. N. R. Agarwal, A. Lucotti, D. Fazzi, M. Tommasini, C. Castiglioni, W. A. Chalifoux and R. R. Tykwinski, *Journal of Raman Spectroscopy*, 2013, **44**, 1398-1410.
36. P. Ramachandran, B.-K. Khor, C. Y. Lee, R.-A. Doong, C. E. Oon, N. T. Thanh and H. L. Lee, *Journal*, 2022, **10**.
37. H. Wang, P. Gao, Y. Wang, J. Guo, K.-Q. Zhang, D. Du, X. Dai and G. Zou, *APL Materials*, 2015, **3**, 086102.
38. B. Singh, Y. Fang, B. C. C. Cowie and L. Thomsen, *Organic Geochemistry*, 2014, **77**, 1-10.
39. A. Kolanowska, G. Dzido, M. Krzywiecki, M. M. Tomczyk, D. Łukowiec, S. Ruczka and S. Boncel, *ACS Omega*, 2022, **7**, 41165-41176.
40. Z. X. Liu, B. B. Chen, M. L. Liu, H. Y. Zou and C. Z. Huang, *Green Chemistry*, 2017, **19**, 1494-1498.
41. H.-X. Wang, W. L. Toh, B. Y. Tang and Y. Surendranath, *Nature Catalysis*, 2023, **6**, 351-362.
42. S. Dey, F. Masero, E. Brack, M. Fontecave and V. Mougel, *Nature*, 2022, **607**, 499-506.
43. Y. Li, H. Zhang, T. Chen, Y. Sun, F. Rosei and M. Yu, *Advanced Functional Materials*, 2024, **34**, 2312970.
44. C. Liang, Y. Chen, M. Wu, K. Wang, W. Zhang, Y. Gan, H. Huang, J. Chen, Y. Xia, J. Zhang, S. Zheng and H. Pan, *Nature Communications*, 2021, **12**, 119.
45. C. Zeng, K. Wang, L. Pan, B. Li, J. Li, L. Zhou, W. Zhang, C. Liang and H. Pan, *Materials Today Nano*, 2021, **16**, 100134.

46. K. Wang, Y. Chen, Y. Wang, C. Liang, H. Huang, Y. Gan, J. Zhang, Y. Xia, X. He and W. Zhang, *Journal of Alloys and Compounds*, 2020, **830**, 154681.
47. D. Qu, M. Zheng, L. Zhang, H. Zhao, Z. Xie, X. Jing, R. E. Haddad, H. Fan and Z. Sun, *Scientific Reports*, 2014, **4**.
48. D. Qu, M. Zheng, P. Du, Y. Zhou, L. Zhang, D. Li, H. Tan, Z. Zhao, Z. Xie and Z. Sun, *Nanoscale*, 2013, **5**, 12272-12277.
49. T. Ogi, H. Iwasaki, K. Aishima, F. Iskandar, W. N. Wang, K. Takimiya and K. Okuyama, *RSC Advances*, 2014, **4**, 55709-55715.
50. R. Tian, S. Zhong, J. Wu, Y. Geng, B. Zhou, Q. Wang and W. Jiang, *Journal of Materials Chemistry C*, 2017, **5**, 9174-9180.
51. J. Yu, C. Liu, K. Yuan, Z. Lu, Y. Cheng, L. Li, X. Zhang, P. Jin, F. Meng and H. Liu, *Nanomaterials*, 2018, **8**.
52. F. Rigodanza, M. Burian, F. Arcudi, L. Đorđević, H. Amenitsch and M. Prato, *Nature Communications*, 2021, **12**.
53. P. C. Hsu and H. T. Chang, *Chemical Communications*, 2012, **48**, 3984-3986.
54. S. Xue, P. Li, L. Sun, L. An, D. Qu, X. Wang and Z. Sun, *Small*, 2023, **19**.
55. D. L. Ruiz, M. d. l. M. Schiavoni, S. L. Laurella, J. M. Giussi, J. J. P. Furlong and P. E. Allegretti, *Spectrochimica Acta Part A: Molecular and Biomolecular Spectroscopy*, 2011, **78**, 1397-1402.
56. J. J. Koo and Z. H. Kim, *Journal of Physical Chemistry Letters*, 2022, **13**, 3740-3747.
57. L. Luo, D. Resch, C. Wilhelm, C. Young, G. Halada, R. Gambino, C. Grey and N. Goroff, *Journal of the American Chemical Society*, 2011, **133**, 19274-19277.
58. W. Ge, J. Liu, X. Zhang, J. He, G. Zhang, M. Sun, S. Kong, Z. Sun, X. Shi, H. Liu and S. Dou, *Advanced Functional Materials*, 2026, **n/a**, e28747.
59. S. Bespalko and J. Mizeraczyk, *Journal*, 2022, **15**, 7508.
60. S. K. Sen Gupta, *Plasma Sources Science and Technology*, 2015, **24**, 063001.
61. M. Liu, Y. Pang, B. Zhang, P. De Luna, O. Voznyy, J. Xu, X. Zheng, C. T. Dinh, F. Fan, C. Cao, F. P. G. De Arquer, T. S. Safaei, A. Mepham, A. Klinkova, E. Kumacheva, T. Filleter, D. Sinton, S. O. Kelley and E. H. Sargent, *Nature*, 2016, **537**, 382-386.
62. L. D. Chen, M. Urushihara, K. Chan and J. K. Nørskov, *ACS Catalysis*, 2016, **6**, 7133-7139.
63. F. M. Alcorn, S. Kumar Giri, M. Chattoraj, R. Nixon, G. C. Schatz and P. K. Jain, *Proceedings of the National Academy of Sciences*, 2024, **121**, e2404433121.
64. J. Yu, J. Yin, R. Li, Y. Ma and Z. Fan, *Chem Catalysis*, 2022, **2**, 2229-2252.
65. W. C. D. Yang, C. Wang, L. A. Fredin, P. A. Lin, L. Shimomoto, H. J. Lezec and R. Sharma, *Nature Materials*, 2019, **18**, 614-619.
66. J. Walia, S. Rashid, G. Killaire, F. Variola, A. Weck and P. Berini, *Optica*, 2021, **8**, 708-709.

67. F. Chen, J. Wu, D. Wang, Y. Xia, Q. Song, Y. Liang, P. Wang, B. Chen, Y. Liang, Y. Yin, Y. Wang, M. Song and G. Jiang, *Chemical Science*, 2024, **15**, 19583-19587.
68. A. R. Rezk, H. Ahmed, T. L. Brain, J. O. Castro, M. K. Tan, J. Langley, N. Cox, J. Mondal, W. Li, M. Ashokkumar and L. Y. Yeo, *The Journal of Physical Chemistry Letters*, 2020, **11**, 4655-4661.
69. A. M. Saitta, F. Saija and P. V. Giaquinta, *Physical Review Letters*, 2012, **108**, 207801.
70. T. W. Marin, C. D. Jonah and D. M. Bartels, *J Phys Chem A*, 2005, **109**, 1843-1848.
71. J. P. Renault, R. Vuilleumier and S. Pommeret, *The Journal of Physical Chemistry A*, 2008, **112**, 7027-7034.
72. K. Lee, E. Park, H. A. Lee, C. Sugnaux, M. Shin, C. J. Jeong, J. Lee, P. B. Messersmith, S. Y. Park and H. Lee, *Nanoscale*, 2017, **9**, 16596-16601.
73. Y. Lu, J. Li, T. Tada, Y. Toda, S. Ueda, T. Yokoyama, M. Kitano and H. Hosono, *Journal of the American Chemical Society*, 2016, **138**, 3970-3973.
74. D. Esrafilzadeh, A. Zavabeti, R. Jalili, P. Atkin, J. Choi, B. J. Carey, R. Brkljača, A. P. O'Mullane, M. D. Dickey, D. L. Officer, D. R. MacFarlane, T. Daeneke and K. Kalantar-Zadeh, *Nature Communications*, 2019, **10**, 865.
75. L. Hu, Z. Yang, W. Yang, M. Hu and S. Jiao, *Carbon*, 2019, **144**, 805-814.
76. K. Zuraiqi, A. Zavabeti, J. Clarke-Hannaford, B. J. Murdoch, K. Shah, M. J. S. Spencer, C. F. McConville, T. Daeneke and K. Chiang, *Energy & Environmental Science*, 2022, **15**, 595-600.
77. Z. Xie, E. Huang, S. Garg, S. Hwang, P. Liu and J. G. Chen, *Nature Catalysis*, 2024, **7**, 98-109.
78. J. Tang, J. Tang, M. Mayyas, M. B. Ghasemian, J. Sun, M. A. Rahim, J. Yang, J. Han, D. J. Lawes, R. Jalili, T. Daeneke, M. G. Saborio, Z. Cao, C. A. Echeverria, F.-M. Allioux, A. Zavabeti, J. Hamilton, V. Mitchell, A. P. O'Mullane, R. B. Kaner, D. Esrafilzadeh, M. D. Dickey and K. Kalantar-Zadeh, *Advanced Materials*, 2022, **34**, 2105789.
79. A. H. Babikir, M. G. M. Ekanayake, O. Oloye, J. D. Riches, K. Ostrikov and A. P. O'Mullane, *Advanced Functional Materials*, 2024, **34**, 2307846.
80. A.-J. Santiago-Cuevas, C.-B. Palacios-Cabrera, E. D. Tecuapa-Flores, I. J. Bazany-Rodríguez, J. Narayanan, I. I. Padilla-Martínez, C. A. Aguilar and P. Thangarasu, *ACS Omega*, 2025, **10**, 13977-14000.
81. Y. Zhu, X. Zhang, L. Zhang, L. Hu, F. Zhang, Y. Wang, Y. Ding, X. Zhu and W. Yang, *Journal of Membrane Science*, 2022, **664**, 121086.
82. B. Domingo-Tafalla, E. Martínez-Ferrero, F. Franco and E. Palomares-Gil, *Molecules*, 2022, **27**.
83. E. Unnikrishnan, A. Krishnamoorthy, S. P. Shaji, A. S. Kamath and M. Ulaganathan, *Current Opinion in Electrochemistry*, 2024, **43**, 101436.
84. Y. Wang, X. Liu, X. Han, R. Godin, J. Chen, W. Zhou, C. Jiang, J. F. Thompson, K. B. Mustafa, S. A. Shevlin, J. R. Durrant, Z. Guo and J. Tang, *Nature Communications*, 2020, **11**, 2531.

85. S. Pandiyan, L. Arumugam, S. P. Srirengan, R. Pitchan, P. Sevugan, K. Kannan, G. Pitchan, T. A. Hegde and V. Gandhirajan, *ACS Omega*, 2020, **5**, 30363-30372.
86. A. Salvi, S. Kharbanda, P. Thakur, M. Shandilya and A. Thakur, *Carbon Trends*, 2024, **17**, 100407.
87. N. Andleeb, S. Zafar, Z. Rahim, M. M. Iqbal, R. Lal and M. A. Farooq, *Planta*, 2025, **262**, 44.
88. M. Gusain, D. Kour, M. Sindhu and A. Bassi, *Next Research*, 2025, **2**, 100788.
89. I. Diwan and P. Khare, *International Journal of Engineering Technologies and Management Research*, 2022, **9**.
90. A. Kim, J. K. Dash, P. Kumar and R. Patel, *ACS Applied Electronic Materials*, 2022, **4**, 27-58.
91. N. Gao, L. Huang, T. Li, J. Song, H. Hu, Y. Liu and S. Ramakrishna, *Journal of Applied Polymer Science*, 2020, **137**, 48443.
92. H. Qu, S. Qian, X. Liu, R. Gao, Z. Wang, C. Zheng and Z. Zhang, *Journal of Building Engineering*, 2022, **52**.
93. T. T. Win, L. Prasittisopin, R. Nganglumpoon, P. Pinthong, S. Watmanee, W. Tolek and J. Panpranot, *Construction and Building Materials*, 2024, **421**.
94. S. Barbhuiya, F. Kanavaris, B. B. Das and M. Idrees, *Journal of Building Engineering*, 2024, **86**, 108861.